Mechanisms for deposition and resuspension of heavy particles in turbulent flow over wavy interfaces

Cristian Marchioli
Centro Interdipartimentale di Fluidodinamica e Idraulica and Dipartimento di Energetica e Macchine, Università di Udine, Udine 33100, Italy

Vincenzo Armenio
Dipartimento di Ingegneria Civile, ed Ambientale, Università di Trieste, 33107, Italy

Maria Vittoria Salvetti
Dipartimento di Ingegneria Aerospaziale, Università di Pisa, Pisa 56122, Italy

Alfredo Soldati[a)]
Centro Interdipartimentale di Fluidodinamica e Idraulica and Dipartimento di Energetica e Macchine, Università di Udine, Udine 33100, Italy

It has been long recognized that turbulent flow over steep waves can produce coherent flow structures of different temporal and spatial scales. In particular, quasistreamwise vortices grow up on the upslope side of the wave and interact with geometry-dependent vortical structures, aligned spanwise and located within the recirculation bubble in the wave trough, thus creating the conditions for the development of a three-dimensional highly turbulent flow field. In this work, we have analyzed the trajectories of $O(10^5)$ small dense particles (either in solid form or in the form of liquid droplets) released into a turbulent air flow over waves precisely to clarify the role of coherent vortical structures in controlling particle deposition and resuspension. The three-dimensional time-dependent flow field at $\mathrm{Re}_\tau=170$ is calculated using large-eddy simulation, and the dynamics of individual different-sized particles is described using a Lagrangian approach. Drag, gravity, and lift are used in the equation of motion for particles that have no influence on the flow field. Particle-wall interaction is fully elastic. Our findings show that different-sized particles interact selectively with vortical flow structures, producing different distribution patterns and dispersion rates qualitatively depending on the particle-to-fluid time-scale ratio. Specifically, we find that quasistreamwise vortices on the upslope side of the wave control particle dispersion and eventual segregation in the flow separation region downstream the wave crest as well as in the shear layer forming behind the wave, just above the separation region. These vortices generate momentum mixing events that also entrain and move particles towards and away from the wavy wall. This process is similar to the sweep/ejection cycle occurring in turbulent flow over a flat boundary layer. © *2006 American Institute of Physics*. [DOI: 10.1063/1.2166453]

I. INTRODUCTION

Deposition and resuspension of inertial particles, droplets, and aerosols in turbulent air flow over wavy solid interfaces are important phenomena in a number of technically relevant engineering and environmental applications. Examples of geophysical importance are the formation of complex bedforms (dunes, ripples, etc.) from sediment deposition and erosion and the coupling flux of heat, mass, and momentum between the atmosphere and the ocean. Other examples include enhancement of heat and mass transfer at low pressure losses in heat exchangers or regenerators and the processes of corrosion and fouling in condensers, evaporators, or heat exchangers.

All these phenomena are characterized by flows occur-ring over complex wall geometries, relatively high Reynolds numbers, and dispersed flow conditions. The fully developed flow over a wavy bottom is a reference configuration that mimics several characteristics of such flows. For instance, the nonbreaking gas-liquid flow over three-dimensional surface waves can be approximated by fluid flow over two-dimensional sinusoidal wave trains if the ratio between the gas and the liquid density is of $O(0.001)$.[1] This is precisely the type of flow we aim to study in the present work. Effects due to changes in wave shape and coupling between the gas and the liquid are not reproduced by our simulations, yet results are still of interest for gas flows over wavy liquids because, to a first approximation, the gas perceives the underneath-flowing liquid much like a solid wall.[1]

The work presented in this paper is part of a broader research project aimed at investigating the physics of particle dispersion in turbulent flows and, where possible, at identifying strategies for particle distribution control.[2–4] Here, we focus on understanding the connection between particle

[a)]Author to whom correspondence should be addressed. Telephone: +39 0432 558020. Fax: +39 0432 558027. Also affiliated with the Department of Fluid Mechanics, CISM, 33100, Udine, Italy. Electronic mail: soldati@uniud.it

transfer mechanisms and turbulence structure for the specific case of fully developed channel flow over wavy walls in the simplest possible setting. In particular, we investigate on the instantaneous mechanisms that lead to particle nonuniform distribution by characterizing the local interaction between the dispersed phase and the large-scale time-dependent flow structures typical of a turbulent boundary layer. These structures span over a wide range of spatial and temporal scales, and are not equally effective in dispersing species. First we will study the evolution of the large-scale coherent vortical structures in the recirculation region of the channel (located in the wave trough) and the quasistreamwise vortices that form near the wavy wall. Even though the wavy wall imposes its wavelength on the quasistreamwise vortices by determining the location of their generation and destruction, these vortices feature several characteristics of those observed in the case of turbulent flow through a flat-walled channel[1,2] and are expected to control particle fluxes toward and away from the wall.[2] Second, we will show that particle fluxes toward and away from the wall are controlled by the large-scale vortical structures in the near-wall region and we will try to quantify the effect of these structures on turbulent deposition and resuspension of species.

Despite the large amount of literature works devoted to the study of the mean and instantaneous turbulent flow structure over wavy walls, there are only few detailed numerical studies dealing with particle dispersion over waves. To the best of our knowledge, extensive studies on the connection between particles and the dynamics of the coherent flow structures are still lacking.

Boersma[5] was the first to perform a direct numerical simulation (DNS) of water flow over a low-amplitude wavy wall in which sand particles were released, subject to drag and gravity. The author obtained indications of large-scale streamwise structures due to a Langmuir-type circulation induced by the small waves on the rippled channel bottom.[6,7] No flow separation (or backflow) was observed, unlike De Angelis *et al.*[1] and Cherukat *et al.*,[8] who did observe flow separation and no Langmuir-type circulation. Boersma[5] observed strong fluctuations of the wall-shear stress occurring upstream of the wave crest, which appear capable of shooting particles back into the flow. As a consequence, particle concentration reaches a maximum on the downstream side of the wave crest and a minimum on the upstream side.

More recently, Chang and Scotti[9] (hereafter referred to as C&S) studied entrainment and resuspension of sediments into a turbulent water flow over ripples. They generated numerically the turbulent flow using a large-eddy simulation (LES), and described sediment motion in a Lagrangian way, analyzing the influence of mobilizing (drag and lift) and stabilizing (gravity) forces. Their main object was to clarify the role of coherent structures in controlling suspension and entrainment of sediments. This is also one of the objects of the present work, which, compared to C&S,[9] addresses further the issue of particle deposition and segregation and has other important differences. First, C&S[9] simulated water flow in which sediments of specific density $S=1.5$ were dispersed, S being the ratio of particle density to fluid density. In the present work, we simulated air flow in which particles with specific density $S \gg 1$ were dispersed. Second, C&S[9] studied particles that are significantly smaller than the Kolmogorov scale based on the mean dissipation rate. Thus, the Stokes numbers are much smaller than those considered here. Also, C&S[9] used sets of 14 400 particles to analyze in detail the connection between particle trajectories and coherent structures. In the present work, we decided to track larger particle sets—100 000 particles—to reduce the variability of particle statistics. This choice should ensure a meaningful quantitative analysis and a reliable statistical description of the phenomena under investigation. Further differences are the upper-boundary condition (no-slip in C&S,[9] free-slip stress-free in the present work) and the bulk Reynolds number, as specified in the following section.

This paper is organized as follows: in Sec. II, we describe the physical problem addressed in this work, and we summarize the details about the LES code used to compute the turbulent flow field and the Lagrangian particle tracker. In Sec. III, the most important results obtained in our simulations are shown and discussed, including the statistics of particle concentration, particle fluxes, and flow structure identification connected to particle distribution. In the final section, conclusions are drawn.

II. PROBLEM FORMULATION

We consider the flow over fixed two-dimensional sinusoidal waves, with geometry and conditions similar to those found in Armenio and Piomelli.[10] In the present idealization, the wave shape is fixed and steady. The fluid is air (density $\rho = 1.2$ kg/m³, kinematic viscosity $\nu = 1.57 \times 10^{-5}$ m²/s), entering the domain with bulk velocity (namely, the average velocity computed along the height of the channel) $U_b = 1.22$ m/s, corresponding to a bulk Reynolds number equal to $\mathrm{Re}_b = U_b H / \nu = 3108$. This Re_b is comparable to that used by Boersma,[5] $\mathrm{Re}_b = 3500$, whereas the bulk Reynolds number used by C&S[9] is $\mathrm{Re}_b = 6500$.

The domain size is given as $2\lambda \times 4/3\pi H \times H$ along the streamwise direction, X, the spanwise direction, Y, and the vertical direction, Z, respectively. The wavelength is $\lambda = 0.06$ m while $H = 0.04$ m is the channel height. The wave shape is taken as $Z(X) = a \cos(kX)$, where $a = 0.005$ m is the wave amplitude and $k = 2\pi/\lambda$ is the wave number. The corresponding slope is $ak \simeq 0.5236$, higher than the threshold value $ak \simeq 0.3$ at which flow separation in the trough of the wave occurs.[7] Also, the amplitude-to-wavelength ratio is large enough to ensure flow separation, which is already observed[11] for $a/\lambda \simeq 0.05$.

All variables have been made nondimensional in terms of wall units (identified by the superscript +), which take $\delta_* = \nu/u_\tau$ and $t_* = \nu/u_\tau^2$ as the reference length and time. Thus, the nondimensional size of the computational domain is $L_X^+ = 510 \times L_Y^+ = 712 \times L_Z^+ = 170$: the streamwise length, L_X^+, is long enough to provide a periodic spatial pattern of the mean streamwise pressure driving the flow, $\nabla_x p$. For an open channel with a wavy lower boundary, the following relationship between $\nabla_x p$ and the friction velocity, u_τ, applies:

$$u_\tau = C_1 \sqrt{\frac{\nabla_x p H}{\rho}}, \tag{1}$$

where the constant C_1 is a correction factor introduced by De Angelis *et al.*[1] to account for the wavy shape of the wall. The constant C_1 is obtained by extrapolating the results given in De Angelis *et al.*[1] and in Salvetti *et al.*[12] for different a/λ ratios. Taking $a/\lambda = 0.083$ as in the present case, we obtain $C_1 = 0.6633$. Reverting Eq. (1), the required pressure gradient is obtained once the friction velocity has been fixed. In the present work, we have $\mathrm{Re}_\tau = u_\tau H/\nu = 170$, which yields $u_\tau = 0.06675$ m/s and $\nabla_x p = 0.119$ Pa/m.

A. Subgrid scale modeling and numerical method

In an earlier paper,[13] the subgrid scale (SGS) modeling and the numerical method have been described in detail. Here, the main features of the approach are recalled briefly in order to make the paper self-contained.

For the incompressible flow considered here, the governing equations are Navier-Stokes (NS) and continuity equations, omitted for sake of brevity. When a filter is applied to these equations, the effects of the unresolved scales appear in the SGS stress tensor as

$$\tau_{ij} = \overline{u_i u_j} - \bar{u}_i \bar{u}_j, \tag{2}$$

in which the overbar denotes the filtering operation and u_i is the velocity component in the ith direction (according to our notation, X_1, X_2, and X_3 correspond to X, Y, and Z, respectively).

The SGS effect is modeled using the dynamic two-parameter model, proposed by Salvetti and Banerjee,[14] in which the SGS stress tensor has the following expression:

$$\tau_{ij} - \frac{\delta_{ij}}{3}\tau_{kk} = -2C\bar{\Delta}^2 |\bar{S}_{ij}| \bar{S}_{ij} + K\left(L_{ij}^m - \frac{\delta_{ij}}{3}L_{kk}^m\right), \tag{3}$$

where $\bar{\Delta}$ is the filter width, $\bar{S}_{ij}$ is the resolved strain rate tensor:

$$\bar{S}_{ij} = \frac{1}{2}\left(\frac{\partial \bar{u}_i}{\partial x_j} + \frac{\partial \bar{u}_j}{\partial x_i}\right), \tag{4}$$

$|\bar{S}_{ij}| = |(2\bar{S}_{ij}\bar{S}_{ij})^{1/2}|$, and $L_{ij}^m = \overline{\overline{\bar{u}_i \bar{u}_j}} - \bar{\bar{u}}_i \bar{\bar{u}}_j$ is the modified Leonard term, representing the resolved part of the SGS stress. The unknown coefficients C and K of Eq. (3) can be computed locally, following the dynamic procedure of Germano *et al.*[14,15]

Computations were made using the finite-volume solver previously described by Zang *et al.*[13] For the purpose of numerical validation, we used the following boundary conditions (see Fig. 1): (1) free-slip stress-free condition at the upper boundary, (2) periodic condition at the box sides, (3) no-slip condition at the wavy lower wall. The governing equations are transformed into a general curvilinear coordinate system, and discretized on a colocated grid using a finite-volume approach.[16] The solver uses two sets of variables, defining Cartesian velocities and pressure at cell centers, and contravariant volume fluxes at the cell faces. A fractional step method is employed to advance in time, and
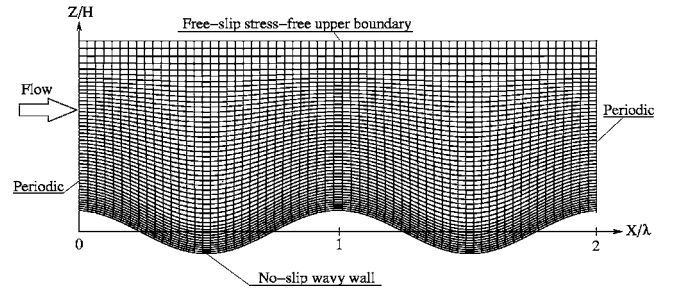

FIG. 1. Schematic of the computational domain.

pressure is obtained by solving a Poisson equation with a multigrid algorithm. Time marching is semi-implicit: the Adams-Bashforth scheme is used for the convective and off-diagonal diffusive terms, whereas the diagonal diffusive terms are treated using the Crank-Nicolson scheme. Overall, the algorithm is second-order accurate both in space and time. Details of the numerical method, extensive validation, and application to different types of flows can be found elsewhere.[13,16] Recently, the same numerical solver and the two-parameter dynamic SGS model have been employed in LES of turbulent flow over sinusoidal waves.[12,17]

The computational grid has $64 \times 64 \times 48$ nodes in X, Y, and Z, respectively. It is uniform in each horizontal direction while nodes along the vertical direction are clustered near the wavy wall following the same procedure as in Salvetti *et al.*[12] (see Fig. 1). With this stretched grid, we put at least five computational points in the so-called *inner region*[18] near the bottom surface. The height of this region, l, can be estimated from the following equation:[18]

$$l \sim 0.5K^2\lambda \ln^{-1}\left(\frac{l}{z_0}\right). \tag{5}$$

In the present case, Eq. (5) gives $l \simeq 0.00128$ m, corresponding to $l^+ \simeq 5.437$ in wall units. The first computational point is approximately at $Z^+ = 0.8$ from the wavy wall. This grid discretization corresponds to a resolution $\Delta X^+ = 7.9$, $\Delta Y^+ = 11.0$, and $\Delta Z^+ = 0.8-7.9$ which, in the near-wall region, compares to the Kolmogorov scale ($\eta_K \simeq 1.6$ in wall units). It also compares to those used in other LESs of turbulent flow over waves[17,19] as well as in DNSs with[5] and without[1,8,20,21] particles. As a consequence of the adopted fine resolution, the SGS contribution to the stress tensor is always very small; this is shown, for instance, in Fig. 2, in which the instantaneous vertical profiles of the single components of the SGS stress tensor, τ_{ij}, normalized by the resolved stresses, $\nu \partial \bar{u}_i / \partial x_j$, are shown at the wave crests [Fig. 2(a)] and troughs [Fig. 2(b)] respectively. Here, Z^+ represents the distance from the bottom wavy wall. Profiles have been computed at several time steps of the simulation averaging along the spanwise direction: those shown refer to the final step. The SGS contribution to the total stress tensor is always smaller than 3% compared to the resolved one, if not negligible. Thus, the subgrid-scale model accounts for only a small portion of the overall dissipation near the wall. Since we do not use any damping function or enforce adherence to
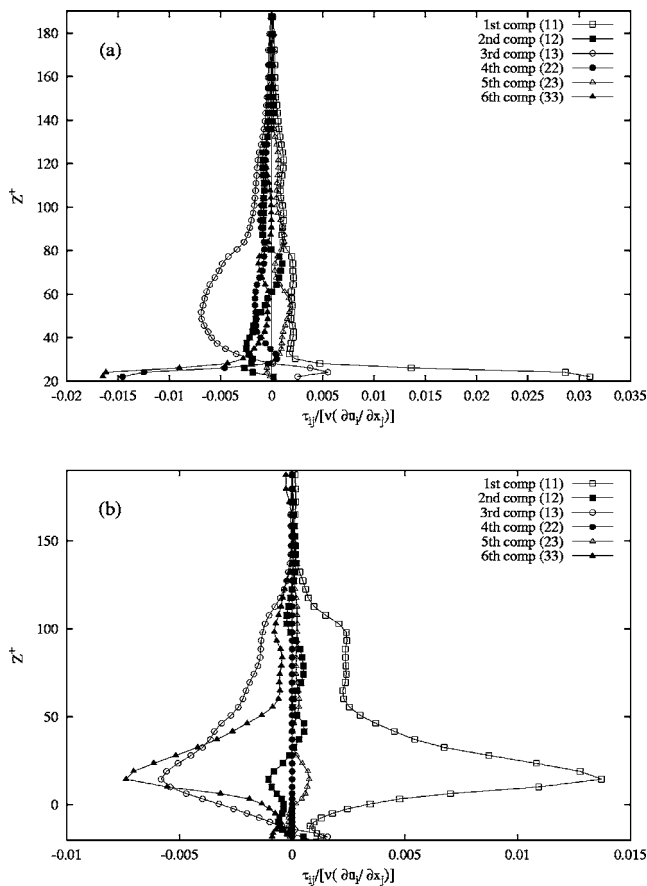
FIG. 2. Vertical profiles of the components of the normalized SGS term, $\tau_{ij}/[\nu(\partial \overline{u}_i/\partial x_j)]$, at (a) wave crests and (b) wave troughs.

TABLE I. Parameters relative to the simulations of particle dispersion. Superscript + identifies nondimensional variables. Note that, in the present study, $\mathrm{St}=\tau_p/\tau_f$ by definition.

τ_p (ms)	$\mathrm{St}(=\tau_p/\tau_f)$	d_p (μm)	d_p^+
0.35	0.1	10.9	0.045
1.76	0.5	24.4	0.104
3.52	1.0	35.0	0.149
7.04	2.0	48.9	0.208

the flow field evolution for 510 time units (about 18 through-flow periods). This period was larger than needed for the calculation of particle dispersion and yet was required to have sufficient data to compute flow field statistics. The nondimensional time step used is $\Delta t^+=0.0357$ and was chosen to ensure stability of the numerical method.

B. Lagrangian tracking

Once we obtained a fully developed flow, we simulated the behavior of $O(10^5)$ rigid particles, either in solid form or in the form of liquid droplets, with density $\rho_p=1000$ kg/m^3. Since the flow above two-dimensional sinusoidal waves is characterized by vortical structures of different size and time scale,[17] we expect that particles of different diameters will interact selectively with these structures, depending on their local Stokes number.[3,4,22,23] We chose to simulate particle diameters ranging from 10.9 to 49 μm, corresponding to particle Stokes numbers ranging from 0.1 to 2.0 time units, respectively. This range includes particles matching the ever-decreasing turbulent flow scales that particles encounter as the wall is approached: in particular, the time scale of the larger particles compares with the Kolmogorov time scale, τ_K, which has an estimated value of about 4 wall time units based on the average dissipation rate and a minimum value of about 2.6 wall units at the wall. Details of particle simulations are reported in Table I. Note that the Stokes number, St, is equivalent to the particle response time $\tau_p=\rho_p d_p^2/18\mu$ made nondimensional using the ratio ν/u_τ^2 as reference time scale for the flow structures. As observed previously,[24] the LES-filtered scales of the flow field do not influence significantly the *statistical* features of particle dispersion when the process is dominated by the well-resolved large-scale structures, as shown in Sec. III.

We calculated the trajectory of each particle by integrating explicitly over time the equation of motion. The following assumptions for particle modelling were made: (i) all particles are noninteracting, nondeformable solid spheres; (ii) particle density is large compared to fluid density; (iii) the effect of the particles on the flow is neglected; (iv) particles are injected into the flow at concentration low enough to ensure dilute system conditions (i.e., negligible particle-particle interaction); (v) virtual mass, pressure gradient, and Basset forces are neglected. Previous works on the importance of the forces acting on particles, based on the equation of motion by Maxey and Riley[25] (see, for instance, Elghobashi and Truesdell,[26] Chung and Troutt,[27] Loth,[28] and Armenio and Fiorotto[29]) reveal that the drag force is $O(\mathrm{St}^{-1})$,

a quadratic stress law,[19] our drag calculations depend mainly on resolved fluid motions.

Also, profiles of the mean flow field and higher-order statistics computed at different X/λ locations (not shown here) appear qualitatively similar to those shown in Hudson *et al.*[11] for separated flow over a slightly larger wave ($2a/\lambda=0.1$) at similar bulk Reynolds number ($\mathrm{Re}_b=3380$). Statistics show good agreement also with those of Henn and Sykes[19] for flow at $\mathrm{Re}_b=10\,450$ over a wave with $2a/\lambda=0.2$.

For the reasons above, we believe that our LES is sufficiently well resolved to capture the dissipation range at $\mathrm{Re}_b=3108$ as well as the overall features of the flow field, particularly the evolution of the larger vortices, which will be discussed later, and the separated shear layer, which plays an important role in turbulence production. *A posteriori* analyses have shown that the cross section of the boundary layer vortices, which have a characteristic time scale, τ_f, ranging about 15–50 wall units, are described by at least nine grid points, thus oversatisfying the Nyquist criterion.

The grid previously described was used to calculate the field evolution starting from the condition of still fluid for a period of about 2384 time units, necessary to achieve statistical convergence. Since the reference time is equal to $T_{\mathrm{ref}}=2\lambda/U_b=28$, this corresponds to 85 times the through-flow period, defined as the time for fluid particles in the middle of the channel to pass through the domain. Then, we calculated

the virtual mass and the pressure gradient are $O(\hat{\rho}^1)$, and the Basset force is $O(\hat{\rho}^{1/2})$, where $\hat{\rho}$ is the ratio of fluid density to particle density. In the present study, $\hat{\rho} \simeq O(10^{-3})$ and St is in the range 0.1–2.0, based on the reference time scale for the fluid (see Table I). Therefore, the neglected terms have a limited effect on the specific flow system examined here, and the equation of motion reduces to a balance of particle inertia and Stokes drag, buoyancy, and lift forces. From Table I, it is apparent that particle diameters considered in our simulations are much smaller than the grid spacing near the wavy boundary.

The equation of particle motion can be written in vector form as

$$\frac{d\mathbf{v}_p}{dt} = \frac{3}{4}\frac{\hat{\rho}}{d_p}C_D(\mathbf{v}-\mathbf{v}_p)|\mathbf{v}-\mathbf{v}_p| + (1-\hat{\rho})\mathbf{g}$$

$$- \xi(\epsilon)\frac{6.46}{12\pi}\frac{d_p}{\tau_p}\left|\frac{\partial\mathbf{v}}{\partial\mathbf{x}}\right|^{0.5}\mathrm{sign}\left(\frac{\partial\mathbf{v}}{\partial\mathbf{x}}\right)(\mathbf{v}-\mathbf{v}_p)\cdot\mathbf{n}, \quad (6)$$

where d_p and $\mathbf{v}_p$ are particle diameter and velocity, $\mathbf{v}$ is fluid velocity, $\mathbf{g}$ is gravity, $\mathbf{n}$ is the unit vector in the wall-normal direction. $C_D = f(\mathrm{Re}_p)$ is the Stokes coefficient for drag, which depends on the particle Reynolds number, $\mathrm{Re}_p = \rho d_p|\mathbf{v}-\mathbf{v}_p|/\mu$. We use the following nonlinear correction for C_D[30] when $\mathrm{Re}_p > 1$:

$$C_D(\mathrm{Re}_p) = \frac{24}{\mathrm{Re}_p}(1 + 0.15\cdot\mathrm{Re}_p^{0.687}). \quad (7)$$

The second term on the right-hand side (rhs) of Eq. (6) represents the lift force. For the range of simulation parameters investigated in the present study, the lift force term is formally of the same order in particle radius as several terms we neglected in the more complete equation of motion derived by Maxey and Riley:[25] thus, the effect of lift on particle deposition rate should be small. However, we decided to verify this assumption performing tests with and without the inclusion of the lift force in Eq. (6). The expression used to model the lift force was first derived by Saffman[31] and corrected by McLaughlin[32] for a small spherical particle in linear shear flows including an additional correction factor $\xi(\epsilon)$ that becomes important when the relative velocity between the particle and the fluid is large. This expression requires less restrictive assumptions with respect to the original Saffman formulation but still neglects wall effects: when the distance of the particle from the bottom wall becomes small compared to particle radius, the actual mechanism of deposition is complicated by the possible rise of surface related phenomena and the formulation without wall effects is not very accurate.[33]

Our tests indicate that the actual influence of the lift force on particles, although small compared to the particle drag in the same direction, might be slightly overestimated, particularly for the smaller inertia particles.

Equation (6) is integrated with an explicit second-order modified Euler method and the integration time step for all particles is one third of the characteristic time of the smallest particles (St=0.1). Further reductions of the time-step size (for instance, by a factor of 4) would result in negligibly

different dispersion statistics.[26] Particles are elastically reflected away from the wall when its center is less than a distance $d_p/2$ from the boundary. Perfect elastic reflection, i.e., where no dissipation occurs during the collision, is at the other extreme with respect to the perfectly absorbing wall model, in which particle kinetic energy is completely lost during the collision. Real cases usually fall in between these limiting situations.

Particles are released within the lower half domain ($Z^+ < 100$). We decided to distribute particles in this nonuniform way since Lagrangian particle tracking is time consuming: to obtain more accurate statistics, we planned to have a larger number of particles in the region where the geometry-dependent flow structures and the quasistreamwise vortices form. Particle initial velocity is set equal to the local fluid velocity, obtained by an interpolation scheme best suited for curvilinear and nonorthogonal grids. The interpolation scheme is based on the Taylor series expansion of the local fluid velocity about the grid point nearest to the particle location. The algorithm uses the fluid velocity at the grid point nearest to the particle, $N=(x,y,z)$, to estimate the local fluid velocity at the instantaneous particle position, $P=(X,Y,Z)$:

$$U_i|_P \approx U_i|_N + \left.\frac{\partial U_i}{\partial x}\right|_N (X-x) + \left.\frac{\partial U_i}{\partial y}\right|_N (Y-y)$$

$$+ \left.\frac{\partial U_i}{\partial z}\right|_N (Z-z), \quad i=1,2,3. \quad (8)$$

The spatial derivatives of U_i in the physical space are transformed onto the computational space as

$$\frac{\partial U_i}{\partial x_j} = \frac{\partial U_i}{\partial \xi_l}\frac{\partial \xi_l}{\partial x_j} = \frac{\partial U_i}{\partial \xi}\frac{\partial \xi}{\partial x_j} + \frac{\partial U_i}{\partial \eta}\frac{\partial \eta}{\partial x_j} + \frac{\partial U_i}{\partial \zeta}\frac{\partial \zeta}{\partial x_j}, \quad i,j,l$$

$$= 1,2,3. \quad (9)$$

The terms $\partial\xi_l/\partial x_j$ are readily available once the computational grid has been generated and only the terms $\partial U_i/\partial\xi_l$ have to be computed. This formulation of the interpolation scheme yields second-order accuracy, the same as that of the NS solver.

To the best of our knowledge, no other work dealing with particle tracking in wavy channel flow (viz., Boersma[5] and C&S[9]) performed interpolation of fluid velocity on a curvilinear grid. Specifically, Boersma[5] tracked particles in the computational rectangular space by means of quadratic interpolation of fluid velocity at 27 neighboring points, whereas C&S[9] exploited the immersed boundary technique[34] for the wavy channel, which allowed the use of sixth-order Lagrangian polynomials.

III. RESULTS AND DISCUSSION

A. Mean flow field, statistical quantities and particle macroscopic behavior

In this section, we will exploit statistical quantities to look at macroscale phenomena characterizing particle behavior in connection with the mean features of the flow field. To this aim, it is important to describe first the dynamics of the flow. The reader is also referred to previous papers (among
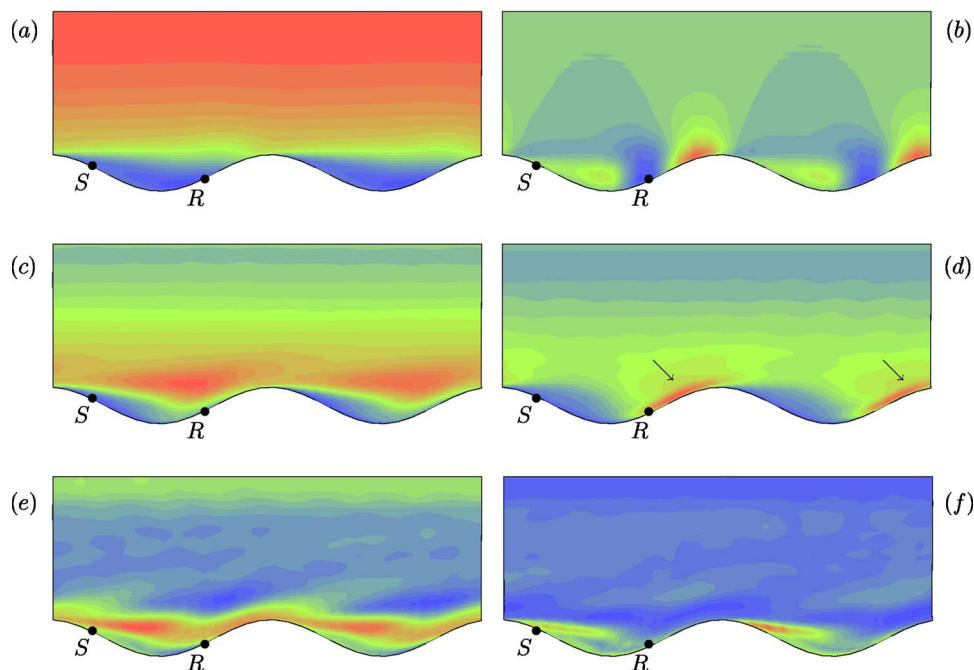
FIG. 3. (Color online). Mean flow field statistics: (a) streamwise fluid velocity, (b) vertical fluid velocity, (c) streamwise turbulence intensity, (d) spanwise turbulence intensity, (e) streamwise skewness, (f) streamwise flatness.

others, see Armenio and Piomelli,[10] Salvetti *et al.*,[12] Calhoun and Street,[17] Henn and Sykes,[19] and Sullivan *et al.*[20] for LES; see De Angelis *et al.*,[1] Cherukat *et al.*,[8] and Nakagawa *et al.*[35] for DNS; see Gong *et al.*,[7] Nakagawa *et al.*,[35] Buckles *et al.*,[36] Kuzan and Hanratty,[37] Nakagawa and Hanratty,[38] and Günther and von Rohr[39] for experiments) in which the flow field forming in various wave configurations is studied in detail.

The flow field may be classified into regions with unique characteristics. First, an outer region and a separation region can be distinguished. The outer region is weakly correlated with the wavy surface and has a large downstream velocity. For a large enough amplitude-to-wavelength ratio and low enough Reynolds numbers, the flow separates behind the wave crest:[37] when separation occurs, the mean flow can be characterized by streamwise periodicity and multiple time and spatial scales persist.

The separated flow is characterized by three regions. The first region is the recirculation bubble, located in the wave trough bounded by the $\Psi=0$ isosurface, with Ψ being the mean streamfunction. The extrema of the recirculation bubble are the separation and reattachment points, defined as locations where the time-averaged velocity gradient at the wall, i.e., the wall-shear stress, is zero.[8,36]

The recirculation bubble is the prominent feature of the mean streamwise velocity field, shown in Fig. 3(a). Gradients are qualitatively displayed using a gray scale, in which dark gray indicates high absolute values whereas light gray indicates values close to zero (red to blue in the online color version).

The recirculation bubble is a region of weak velocity gradients, whereas strong velocity gradients occur on the upslope boundary and crest region of the wave, as well as near the lee side of the crest. At the reattachment point, indicated

with the letter R and located at a distance $x/\lambda=0.72$ downstream of the wave crest, boundary layers form along the wall. In particular, the boundary layer in the downstream direction originates from the reattachment point, grows and accelerates under strong favorable pressure gradients, progressing to the next separation point, where the maximum production of kinetic energy occurs.[8] Once at the separation point, indicated with letter S and located at a distance $x/\lambda=0.16$ downstream of the wave crest, the boundary layer lifts away from the surface as a free shear layer, in response to the adverse pressure gradient encountered when the flow cross section increases again. The detached layer spreads rapidly downstream of separation and may continue at a higher level over the next crest where a new layer may form beneath.

Contours of the mean vertical velocity, shown in Fig. 3(b), provide evidence of the recirculation bubble as positive vertical velocities on the downslope portion of the wavy surface. Positive vertical velocities are also found downstream of the wave crest: here, the fluid is pushed relatively powerfully upward by the upslope portion of the wavy surface and recovers downward much more gently over a longer period.

Contour plots of streamwise and spanwise fluctuations of the fluid velocity are shown in Figs. 3(c) and 3(d), respectively. In the streamwise direction [see Fig. 3(c)], high fluctuations are found in the free shear layer. In the spanwise direction [see Fig. 3(d)], large fluctuations occur in the so-called *impact zones* (indicated by black arrows): these are very thin layers located downstream of the wave troughs, where the flow is going toward the wave crest and reattaches. Here, spanwise fluid velocity fluctuations become comparable to streamwise fluctuations in the shear layer,[10] and seem related to persistent flow structures characterized by a relatively small scale in the spanwise direction, though large
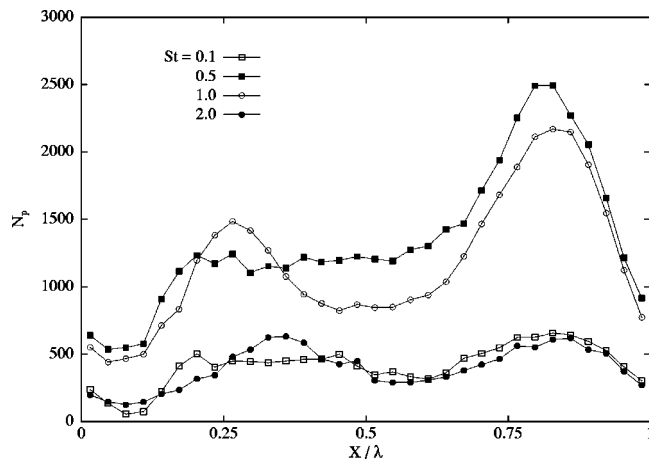
FIG. 4. Particle number density distribution at impact with the wall (N_p) along the streamwise direction (X/λ).

FIG. 5. St=1.0 particle number density distribution at impact with the wall (N_p) along the spanwise direction (Y/H) at different streamwise locations (X/λ).

in the streamwise direction.[17] The lowest spanwise intensities occur in the recirculation bubble.

Contour plots of skewness and flatness of the streamwise velocity component are shown in Figs. 3(e) and 3(f), respectively. A region of high skewness occurs just downstream of the crest, reaching its maximum around the separation point. Large negative values of skewness occur in proximity of the wave surface over the backflow region, whereas near-wall positive skewness seems to be associated with attached, forward-moving fluid. This is consistent with the view that near-wall velocity fluctuations are caused by a fast-moving fluid being mixed down from above. Comparing Figs. 3(e) and 3(f), it is apparent that large positive flatness correlates well with large positive skewness in the backflow region. However, LES profiles show slight sensitivity to resolution (especially for the flatness) since only the resolved velocity fluctuations are considered.[19]

As mentioned, our object here is to link the mean features of the flow field just reviewed to particle macroscopic behavior. To this end, in Fig. 4 we show particle number concentration at impact with the wall (N_p) along the streamwise direction (X/λ). Profiles have been computed dividing the wavelength into equally spaced bins and counting the number of particles hitting the wall within each bin over the last 350 t^+ of the simulations. Only particles whose velocity has become independent of the initial conditions were considered: then, particle statistics can be computed as a function of both wall-normal and spanwise directions without any effect of the imposed initial conditions. In the present case, decorrelation is achieved by particles travelling a distance equal to eight times the wavelength before impact.[40]

Profiles shown in Fig. 4 are averaged in space along the spanwise direction and develop two peaks. The first, and lower, peak occurs in the recirculation bubble, and is characterized by small mean flow and low turbulence intensities. At the boundaries of this region, however, skewness and flatness are relatively large, suggesting the existence of an intermittent mixing of fast-moving flow to the wall, possibly associated with the passage of shear-layer vortices overhead. The second, and higher, peak occurs in the upslope part of
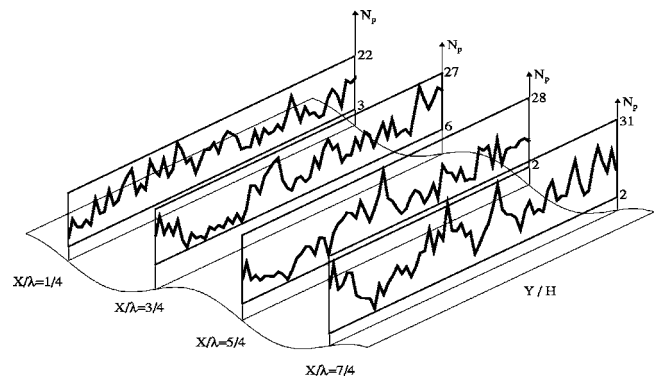
the wave, which is characterized by the impact zone. Large turbulence fluctuations and streamwise skewness in this zone indicate that particle motion is associated with the attached, forward-moving fluid.

While their location appears almost unaffected by the particle time scale, the intensity of the two peaks depends strongly on the selective particle response to the underlying flow field. Specifically, the number density is maximum for particles with intermediate inertia (namely St=0.5 particles, black squares, and St=1.0 particles, open circles), which are likely to respond best to the specific scales of the coherent vortical flow structures and sample preferentially the flow field. The preferential sampling by particles with small inertia (St=0.1, open squares) is weaker: small particles are able to respond promptly to almost all turbulence fluctuations and their deposition location distributes more homogeneously. The macroscopic outcome is a rather flat profile, which is observed also for larger inertia particles (St=2.0, black circles) yet for an opposite reason. Particles respond only if their behavior is consistent with the motion and effects of coherent wall structures. Once in the near-wall region, the characteristic scale of such structures decreases progressively as they lie closer to the wall, becoming too small to affect the dynamics of particles with large enough inertia. The inertial filtering induced by particles weakens their local interaction with coherent wall structures and flattens the number density distribution profile.

From Fig. 4, the effect on particle dynamics of both the recirculation region and the shear layer, which are long-lived flow structures, is apparent: only few particles are able to hit the wall at the crest or at the trough. However, the local instantaneous effect of less-persistent vortical flow structures can not be neglected: for instance, the very low particle concentrations observed just above the wave crest are probably due to strong shear-stress fluctuations at the wall upstream of the wave crest, which continuously act to shoot particles back into the flow. Furthermore, the effect of mean flow structures on particle dynamics is not evident when one looks at particle number density distribution at impact (N_p) along the spanwise direction (Y/H). Profiles are shown in Fig. 5 for the St=1 particles at four streamwise locations (X/λ) along the wave. The vertical axes report the min/max
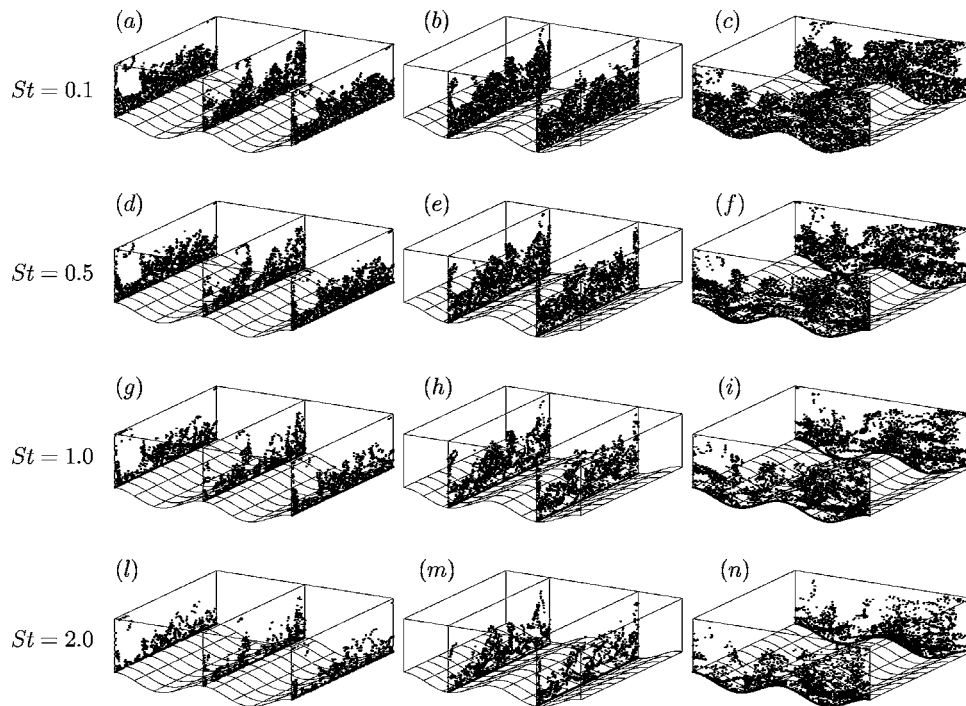
FIG. 6. Perspective view of instantaneous particle distribution. (a), (d), (g) and (l): instantaneous distribution of particles crossing (Y,Z) planes perpendicular to the mean flow located at the wave crests. (b), (e), (h) and (m): instantaneous distribution of particles crossing (Y,Z) planes perpendicular to the mean flow located at the wave troughs. (c), (f), (i) and (n): instantaneous distribution of particles crossing (X,Z) planes perpendicular to the transverse direction.

value of N_p found at each X/λ location. A large number of sharp peaks is observed, which occur at spatial scales smaller than those of the long-lived mean flow structures. These peaks, which are observed also for the other particle sets, must be originated by smaller and less-persistent vortical structures populating the near-wall region. Our hypothesis, which will be verified in the following section, is that these structures are the quasistreamwise vortices on the upslope side of the wave.

B. Instantaneous turbulence structure over the waves and particle distribution

In Fig. 6 we show the perspective view of instantaneous particle distribution for all particle sets. For clarity of presentation, only a fraction of the dispersing particles is plotted. Figures 6(a), 6(d), 6(g), and 6(l) show particles crossing (Y,Z) planes perpendicular to the mean flow located at the wave crests. Figures 6(b), 6(e), 6(h), and 6(m) show particles crossing (Y,Z) planes perpendicular to the mean flow located at the wave troughs. Figures 6(c), 6(f), 6(i), and 6(n) show particles crossing (X,Z) planes located at the sides of the computational domain along the spanwise direction.

From these figures, it is apparent that the instantaneous particle distribution is highly nonhomogeneous since regions where particles tend to cluster are followed by regions almost depleted of particles. As expected, some particles deposit at the wavy wall under the action of the gravitational pull. Yet a significant proportion of particles, initially released within the lower half domain, is driven upwards by near-wall turbulent coherent structures forming elongated billows and necklaces. This indicates the existence of com-

peting gravitational and turbophoretic-like mechanisms in wall transfer of inertial particles. Gravity decouples particle behavior from the turbulence structure with effects on particle wall-normal distribution and deposition rates much larger for larger particles. Still, the transfer mechanisms for particles with small inertia ($St \leqslant 2$) are strongly dominated by the action of the near-wall turbulent structures. This behavior is common to all particle sets considered in this study and is intimately connected to the dynamical features of the instantaneous velocity field, which rarely resembles the pattern indicated by the mean velocities. In particular, there are similarities with the process of particle dispersion in flat channel flow, where particle behavior is governed by the near-wall coherent vortices.[2] A snapshot of these vortices for the case of separated flow over waves is shown in Fig. 7, where the streamline rotation vector, $\mathbf{\Omega}$, is used for visualization.[41] This vector has been widely used to measure vortices: it represents the strength and direction of the streamline rotation and may be established on the basis of the eigenvectors for each complex eigenvalue of the fluid velocity gradient tensor, $\partial u_i / \partial x_j$.

The prominent structures in Fig. 7 are the quasistreamwise vortices that begin in the upsloping impact zone, project downstream over the trough, and eventually lose their identity somewhere over the trough. Less frequently, an arch structure similar to those described in the literature on coherent structures over a flat boundary layer can be found (see the black circle). Rarely, small spanwise vortices can be observed.[17]

Quasistreamwise vortices control particle transport in a number of boundary layer-type flows.[2,42] The wavy wall adds
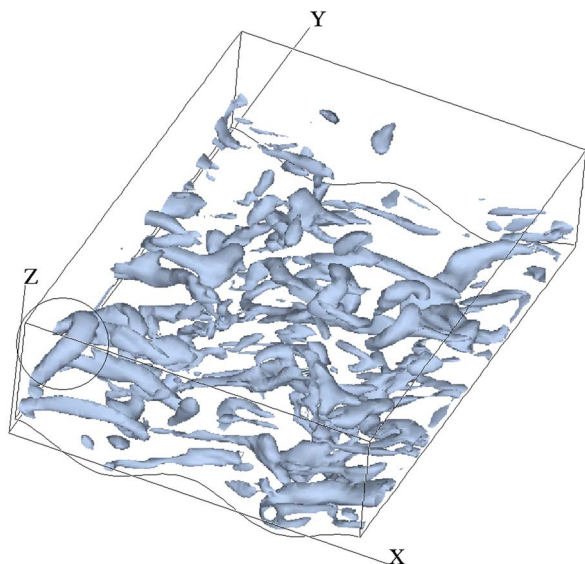
FIG. 7. (Color online). Near-wall instantaneous vortical structures for turbulent flow over wavy walls.

a degree of complexity: even for the same flow conditions, turbulence near a wavy surface is different from turbulence near a flat wall. First, long wall vortices are not observed. The extent of the quasistreamwise vortices appears to scale with wavelength, which *organizes* the behavior of the wall layer by affecting vortical structures regeneration mechanisms. For a flat wall there is no such characteristic scale and turbulence structure is only related to internal spatial scales arising from the mean shear rate.

Second, turbulent structures emanating in the boundary layer upstream of the recirculation bubble move forward into the separated shear layer formed downstream of the wave crest.[8] An interesting aspect of the shear layer is its interruption by velocity bursts.[8,37] A thin layer of streaky (both low-speed and high-speed) fluid develops and propagates over the crest of the wave and over the recirculation bubble. Here, the wall layer is very active: strong ejections occur, which are transported by the mean flow over the separation region and eventually impact the wall at the next reattachment re-
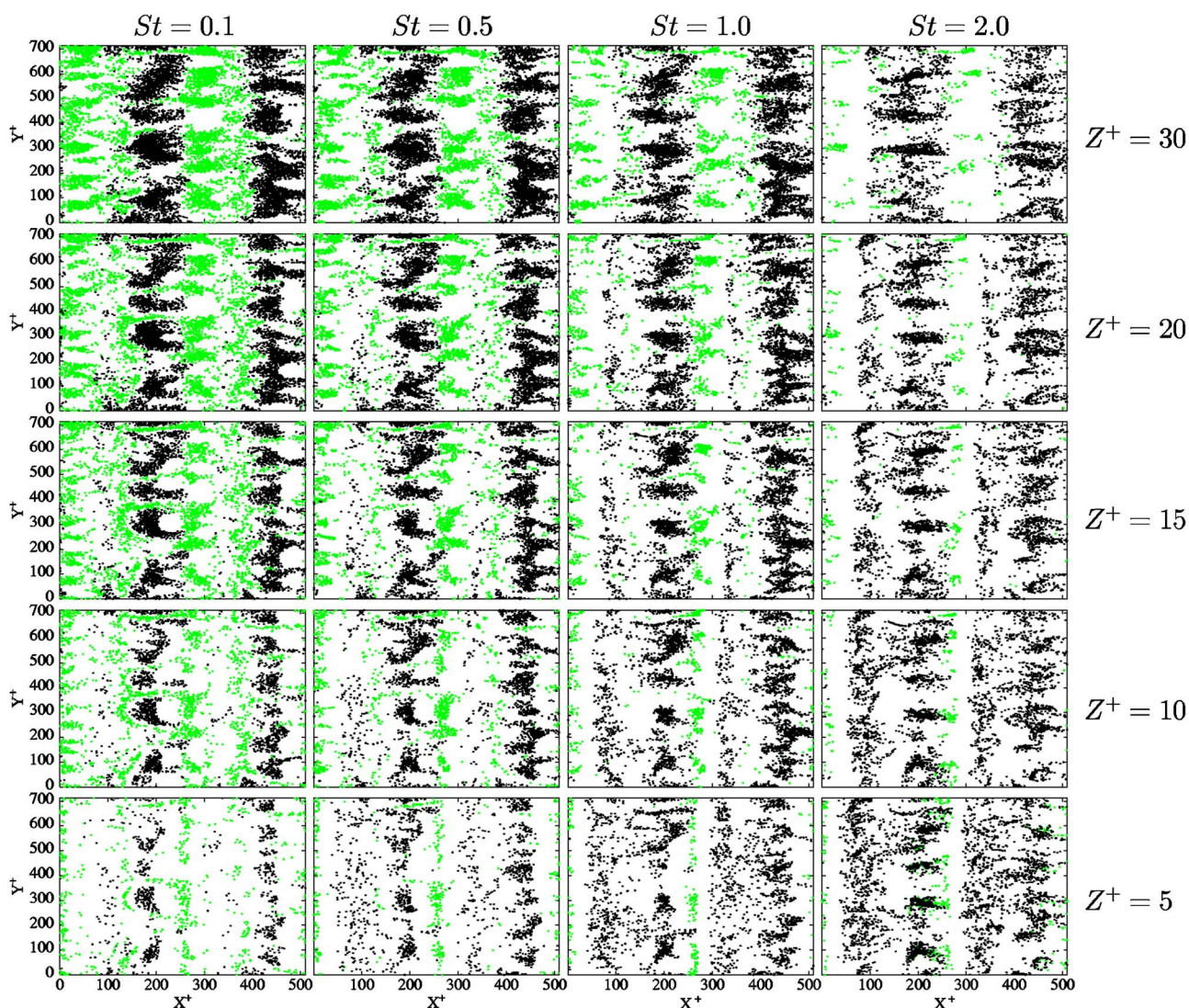

FIG. 8. (Color online). Top view of instantaneous distribution of particles crossing a sinusoidal monitor surface located at different heights from the bottom wall ($Z^+=5$, $Z^+=10$, $Z^+=15$, $Z^+=20$, $Z^+=30$). Figures relative to the each particle set are displayed in the same column. Figures relative to the each monitor surface are displayed in the same row. Snapshots are taken at time $t^+=250$. The mean flow is from left to right. Black particles have negative vertical velocity and move downward, light gray particles (green in the online color version) have positive vertical velocity and move upward.
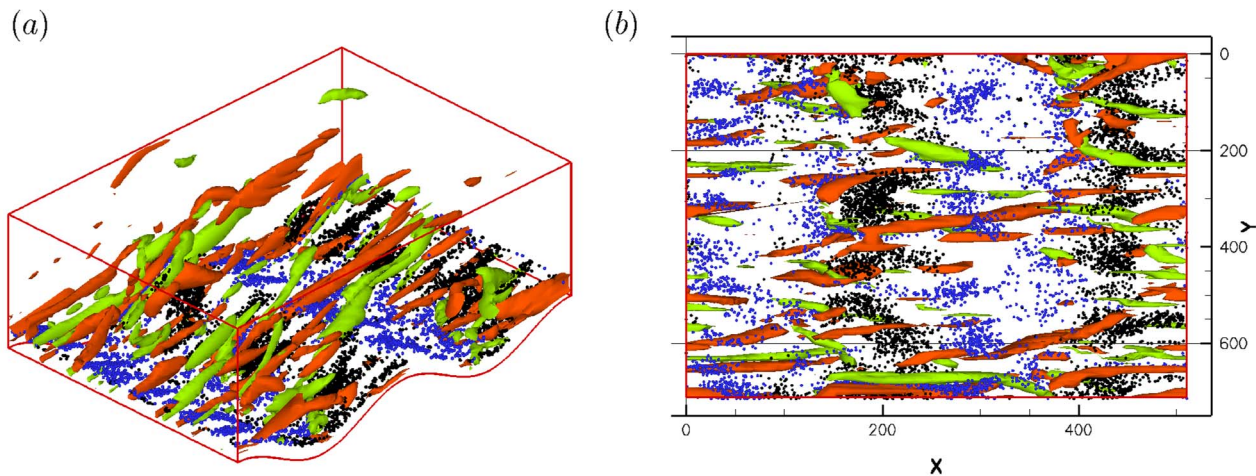
(a) (b)

FIG. 9. (Color online). Snapshot of $St=0.1$ particle distribution and coherent vortical structures in the near-wall region at time $t^+=250$. Light gray Ω isosurfaces (green in the online color version) indicate counterclockwise-rotating vortices, dark gray Ω isosurfaces (red in the online color version) indicate clockwise-rotating vortices. Particle color code is the following: dark gray particles (blue in the online color version) have negative vertical velocity and move downward, black particles have positive vertical velocity and move upward. For visualization purposes, only those particles crossing a sinusoidal surface at a distance $Z^+=20$ from the bottom wall are considered: (a) perspective view, (b) view from the bottom of the channel up.

gion, somewhat like sweeps. The kinetic energy of the impacting fluid partly redistributes to the spanwise direction and partly generates high shear stress downstream of the reattachment point [see Fig. 3(d)]. High shear stress regions form where streaky structures and quasistreamwise vortices are seen to initiate. As shown by Calhoun and Street,[17] quasistreamwise vortices create columnar motions carrying fluid between the wave surface and the shear layer. Billows of slower-moving fluid extend upward and their upper part tends to lose intensity, being absorbed into the surrounding fluid which moves faster. In the recirculation bubble, bursts of slower-moving fluid into the outer region also occur, though not as regularly or with the same billow structure. The effect of the wavy wall is to organize ejections so that they occur mainly over the trough.[17]

Such strong intermittent fluid motions qualitatively resemble the sweep/ejection cycle characteristic of turbulence regeneration in the boundary layer occurring over flat walls. However, experimental observations[35] show that significant quantitative differences between the turbulence statistics for flow over flat and wavy surfaces appear in the quadrant analysis of the Reynolds shear stress. Wavy surfaces show much smaller contributions from sweep events and much larger contributions from large-scale ejections of low-momentum fluid from the trough of the waves. This is consistent with the large negative values of the skewness in the streamwise direction observed in Fig. 3(e) and with the large positive values of the skewness in the spanwise direction (not shown here).

C. Mechanisms for particle deposition and resuspension

In Fig. 8, we provide a qualitative representation of the instantaneous particle fluxes toward and away from the wall, taken at time $t^+=250$. We consider all particle sets and we focus on five monitor wavy surfaces located at a fixed dis-

tance from the bottom wall ($Z^+=5$, $Z^+=10$, $Z^+=15$, $Z^+=20$, and $Z^+=30$, respectively). Particles crossing each surface are characterized with their vertical velocity w_p: black particles have $w_p<0$ and are directed toward the wall, and light gray particles (green in the online color version) have $w_p>0$ and are directed toward the outer flow.

Several observations can be drawn from Fig. 8. First, most of the descending (black) particles cross the monitor surfaces above the upslope side of the wave, where the quasistreamwise vortices start developing. In turn, most of the ascending (light gray) particles cross the monitor surfaces above the downslope side of the wave, where quasistreamwise vortices have detached from the bottom wall to follow the shear layer. In this region, the time scale of quasistreamwise vortices, which depends linearly on wall distance and increases progressively as the structure lies farther from the wall, becomes much larger than the Kolmogorov scale: thus, vortices are much more robust and effective in controlling particle motions. The scenario is qualitatively similar for small and intermediate particles ($St=0.1$, 0.5, and 1.0), while the flow is not energetic enough to lift a significant proportion of heavy particles ($St=2.0$): in this case, particle deposition due to gravity outbalances particle resuspension due to the action of turbulence coherent structures.

Second, particles distribute nonhomogeneously and collect into filaments separated by empty regions. Most likely, this is a consequence of local small-scale interactions occurring between the particles and the quasistreamwise vortices: black particles are likely to be entrained by the descending flow close to the downwash sides of the vortices and tend to collect into necklaces with a spanwise body and streamwise legs; light gray particles (green in the online color version) are likely to be entrained by the ascending flow found in between the vortices and collect in filaments that are streamwise oriented most of the time. However, the shape of filaments and necklaces may change with particle inertia.
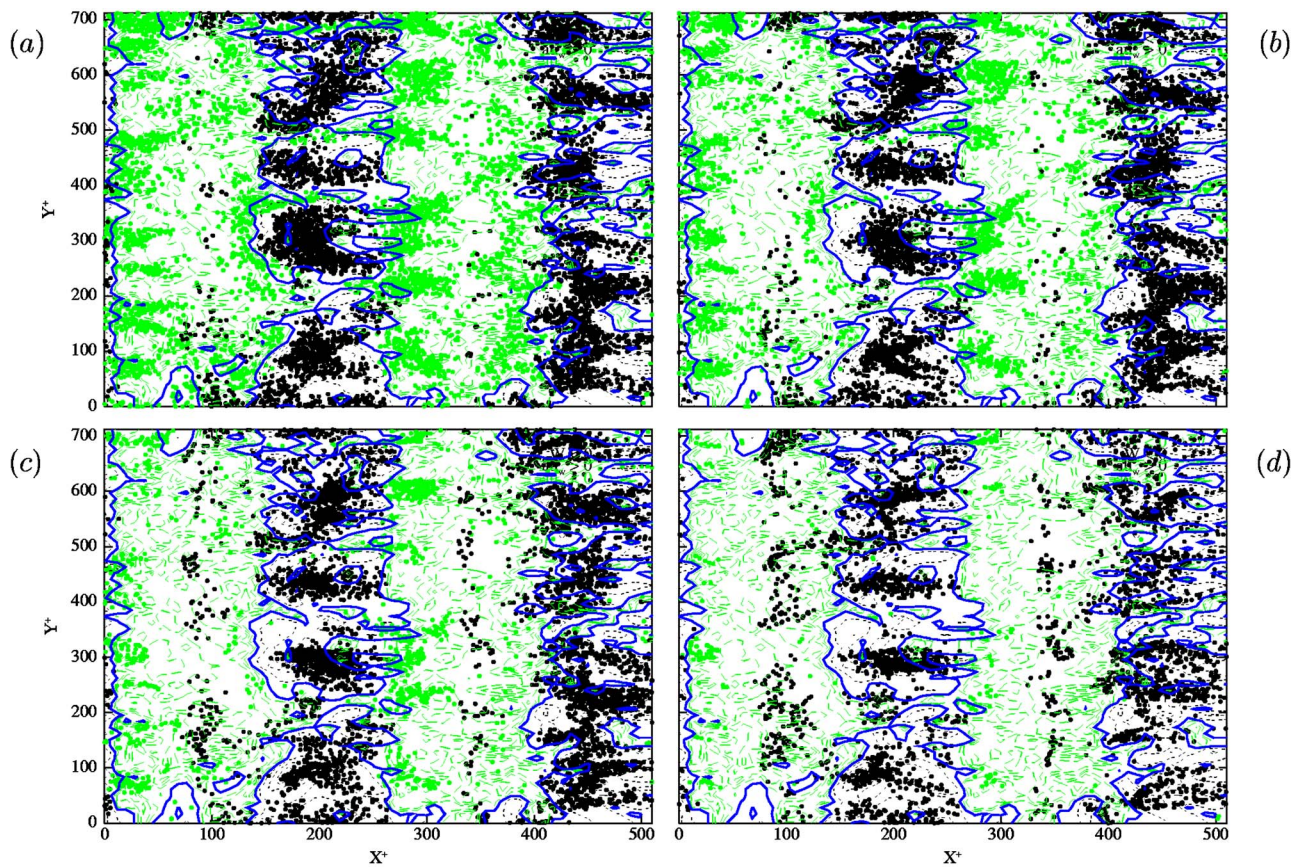
FIG. 10. (Color online). Instantaneous correlation between wall-shear stress distribution and particle fluxes toward the wall and away from the wall at a sinusoidal surface located at $Z^+=10$ from the bottom wall. Snapshots are taken at time $t^+=250$. The mean flow is from left to right. Black particles have negative vertical velocity and move downward, light gray particles (green in the online color version) have positive vertical velocity and move upward. The distribution of wall-shear stress τ_w is coded as follows: the dark gray solid contour (blue in the online color version) indicates the mean value, $\bar{\tau}$, of τ_w at the time step considered, black dashed contours indicate regions where $\tau_w > \bar{\tau}$, light gray dashed contours (green in the online color version) indicate regions where $\tau_w < \bar{\tau}$. (a) St=0.1 particles, (b) St=0.5 particles, (c) St=1.0 particles, (d) St=2.0 particles.

Third, the effect of local particle-vortex interactions is less intense when approaching the wall. As the monitor surface lies closer to the bottom boundary, particle clustering is less evident and filaments and necklaces lose coherence and break up, this process being affected also by particle inertia.

All these observations seem to agree well with previous results obtained by C&S,[9] stressing the importance of near-wall turbulent coherent structures in controlling sediment suspension and reentrainment. To provide evidence of this role, we have to link macroscopic transport phenomena to the dynamics of the coherent structures. To this end, we have examined a large number of snapshots showing the action of quasistreamwise vortices on particle transfer in the wall region. We show one of these in Fig. 9, which provides a perspective view [Fig. 9(a)] and a view from the bottom of the channel up [Fig. 9(b)] of quasistreamwise vortices at the same time instant of Fig. 8. Superimposed is the instantaneous distribution of St=0.1 particles at $Z^+=20$ already shown in Fig. 8. Light gray Ω isosurfaces (green in the online color version) indicate counterclockwise-rotating vortices, and dark gray Ω isosurfaces (red in the online color version) indicate clockwise-rotating vortices. The particle color code is the following: black particles have $w_p<0$ and move downward, and dark gray particles (blue in the online

color version) have $w_p>0$ and move upward. The action of the vortices in transferring the black particles to the wall and the dark gray particles away from the wall is apparent: a vortex can be found at or near the preferential locations where particles penetrate and exit the wall layer. For brevity, we do not show the same visualizations for intermediate and large particles: we just mention that particle inertia acts to decouple particle behavior from the dynamics of the turbulence structures, thus decreasing the extent of the interaction.

Bursting events are also important. In Fig. 10, we correlate the instantaneous position of particles directed toward the wall and away from the wall, characterized by $w_p<0$ (black dots) and $w_p>0$ (light gray dots here, green dots in the online color version), respectively, with the location of bursting sweep/ejection events, all projected in the (X,Y) plane. Sweeps represent descending flow close to the down-wash sides of the vortices and are characterized by black dashed isocontours corresponding to high shear stress regions at the wall. Ejections represent ascending flow found in between the vortices and are characterized by light gray dashed isocontours (green in the online color version) corresponding to low shear stress regions at the wall. High and low shear stress regions have been separated by a crossover
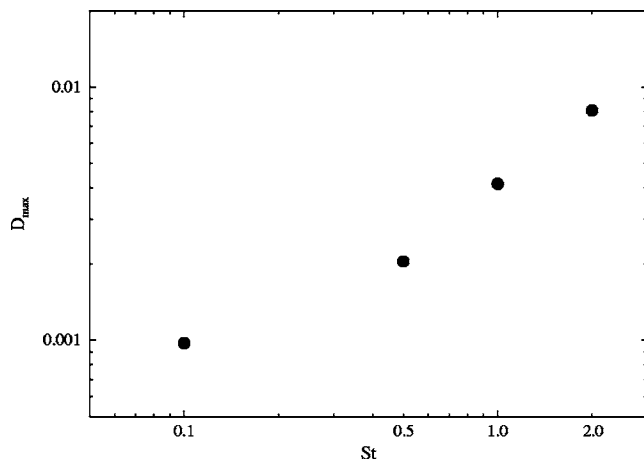
FIG. 11. Dependence of particle distribution peak deviation from randomness, D_{max}, on particle Stokes number, St.

level equal to the mean value $\bar{\tau}$ of the wall-shear stress, represented by the dark gray solid contour (blue in the online color version) in Fig. 10. We chose a monitor surface located at distance $Z^+=10$ from the wavy wall at time $t^+=250$ as reference. Focusing on the smaller particles [St=0.1, Fig. 10(a)], there is evidence of a strong correlation between particles with $w_p<0$ and sweeps, since only a small fraction of the particles falls out of sweep regions. Also, the position of the particles with $w_p>0$ correlates well with the instantaneous position of ejections. As in C&S,[9] the area of the wave over which particle resuspension occurs most actively seems to be the wave upslope, characterized by large wall-shear stress and high turbulent fluctuations. In turn, the wave downslope and the trough, characterized by small wall-shear stress and low turbulent fluctuations, seem to be the areas where deposition occurs most actively. The same type of visualizations for the larger particle sets [Figs. 10(b)–10(d)] confirm the qualitative results of Fig. 10(a), even though spatial correlations become slightly weaker due to an increase of particle inertia.

Visualizations provided in Figs. 8, 9 and 10 demonstrate qualitatively that particle transfer fluxes can be explained only by considering the combined action of the geometry-dependent long-lived flow structures together with large-scale quasistreamwise vortices and related bursting events, which affect particle dynamics on smaller spatial and time scales. Visualizations also show that particles respond selectively to the turbulent flow structures depending on their inertia, and that particle response can be correlated to the instantaneous distribution of the shear stress at the wall.

To investigate further on the mechanisms by which particles are transferred in the vertical direction, we analyze quantitatively the correlation between coherent structures and particle position. To this end, it is useful to define a quantitative measure of the nonrandomness of particle distribution scaled with the particle Stokes number. The log-log plot of Fig. 11 shows the peak deviation from a random particle distribution, D_{max}, as a function of St. This plot quantifies the degree of particle preferential concentration regardless of the length scale on which it occurs.[43] D_{max} has

been computed as $(\sigma-\sigma_{\text{Poisson}})/m$, where σ and σ_{Poisson} represent respectively the standard deviation for the particle number density distribution and the Poisson distribution in the buffer layer $(5<z^+<30$ from the bottom wall) and m is the mean particle number density.[44–46] As in Rouson and Eaton,[44] "random" is defined as the situation in which any given particle is equally likely to appear in any given computational cell: under such conditions, one can show that the particle number distribution approaches a Poisson distribution.

Our results indicate that the larger the particle time scale, the higher the D_{max}. We remark here that no maximum is observed for the range of particle time scales investigated in this study, whereas Fig. 4 shows a peak of number density concentration upon impact along the waves for intermediate values of the Stokes number. In our opinion, this happens because particle deposition is dominated by vortical structures with a time scale, τ_f, larger than the Kolmogorov time scale, τ_K, for all particle sizes investigated. This observation is in agreement with a similar analysis performed recently by Picciotto *et al.*[4] for plane channel flow at $Re_\tau=150$, in which it was demonstrated that (i) the maximum preferential concentration in the near-wall accumulation regions of flat turbulent boundary layers occurs for particles with St about 25 and that (ii) particle dynamics in the near-wall region is controlled by flow structures with $\tau_f\simeq25$, thus much larger than τ_K. A possible development of the present work would be to determine a detailed trend in the behavior of D_{max} for larger particle time scales to find the point of peak D_{max}.

As particles tend to segregate depending on their size, it is useful to define an integral parameter to correlate particle selective distribution with coherent structures on a statistical base. Specifically, in different flow configurations, quasipure advection[22] was observed for a particle time scale very small compared to that of the flow structures, whereas segregation and preferential accumulation has been observed when the time scales become comparable.[3] Here we aim at identifying the flow scales that control the dispersion and segregation processes observed in Figs. 6 and 8.

Maxey[47] and Squires and Eaton[48] found that the concentration of inertial particles in a turbulent flow correlates well with the strain rate and the vorticity fields. In particular, Squires and Eaton[48] studied the effect of turbulence on particle concentration in an isotropic turbulent flow using DNS and observed that inertial particles collect preferentially in regions of low vorticity and high strain rate, this effect decreasing for increasing particle inertia. An adequate tool to identify regions of simultaneous high strain rate and low vorticity is the second invariant Q of the velocity gradient tensor $\partial u_i/\partial x_j$, defined as[49]

$$Q = \frac{1}{2}\left[\left(\frac{\partial u_i}{\partial x_i}\right)^2 - \frac{\partial u_i}{\partial x_j}\frac{\partial u_j}{\partial x_i}\right]$$

$$= -\frac{1}{2}\frac{\partial u_i}{\partial x_j}\frac{\partial u_j}{\partial x_i} = \frac{1}{2}(\Omega_{ij}\Omega_{ij} - S_{ij}S_{ij}), \quad (10)$$

where the rhs of Eq. (10) holds for incompressible flow fields. Here $\Omega_{ij}=\frac{1}{2}(\partial u_i/\partial x_j - \partial u_j/\partial x_i)$ and $S_{ij}=\frac{1}{2}(\partial u_i/\partial x_j + \partial u_j/\partial x_i)$ are the antisymmetric and symmetric components
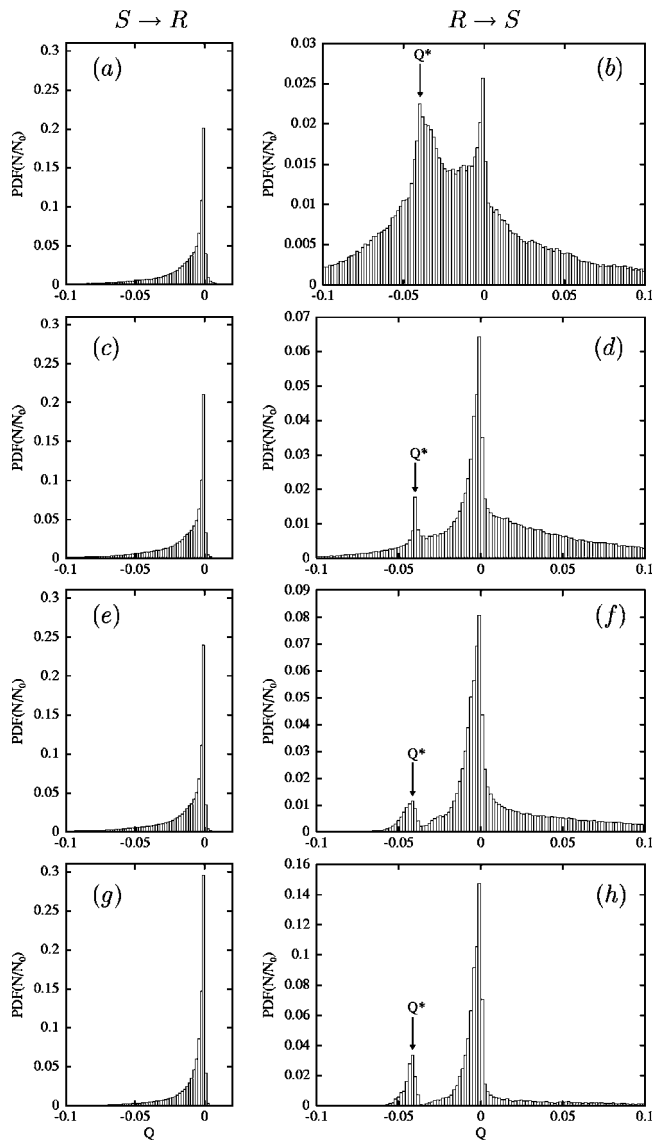
FIG. 12. Viscous sublayer ($Z^+ < 5$) joint PDF of Q conditionally sampled at a particle position. (a) and (b) St=0.1 particles, (c) and (d) St=0.5 particles, (e) and (f) St=1.0 particles, (g) and (h) St=2.0 particles.

of the velocity gradient tensor. Specifically, Q represents the local balance between vorticity (related to Ω_{ij}) and the strain rate (related to S_{ij}): a fluid point characterized by positive values of Q indicates the presence of high vorticity, whereas negative values of Q indicate flow regions dominated by straining motions.

In Fig. 12 we show the probability density function (PDF) of the particle concentration number, PDF(N/N_0), as a function of Q. Calculations were made considering a near-wall fluid slab 20 wall units thick as control volume. Particles pertaining to such control volume were divided into two distinct populations: those located within the recirculation bubble (from S to R in Fig. 3) and those located along the remaining portion of the wavy wall (from R to S in Fig. 3). This choice was made to discriminate among the effects of different classes of coherent vortical structures on particle

preferential distribution. PDFs were computed for each population over a nondimensional time period equal to $t^+ = 250$.

The PDFs for particles entrained in the recirculation bubble are shown in Figs. 12(a), 12(c), 12(e), and 12(g), relative to St=0.1, St=0.5, St=1.0 and St=2.0 particles, respectively. Each PDF is skewed towards negative values of Q and develops a sharp peak centered at $Q=0$, the height of which is proportional to the percentage of particles not actively involved in turbulent deposition and resuspension mechanisms. The value $Q=0$ is the most probable within the time window considered. In principle, this is true even for randomly distributed particles, because Q has zero expectation and mode. Yet, preferentially distributed particles produce narrower PDFs, characterized by a massive clustering of samples around the mean value.

According to the classification by Chong *et al.*,[49] the value $Q=0$ corresponds to low-vorticity and low-strain regions, characterized by absence of flow structures. We can argue that, in the near-wall region within the recirculation bubble, strongly geometry-dependent vortical regions fling a large proportion of particles out of the vortex core.[44] As a consequence, particles sample preferentially $Q=0$ regions. A similar preferential sampling by the dispersed phase has been observed in plane channel flow[44] and also in confined turbulent round jet,[3] which, however, is characterized by coherent rollers of larger scale.

The PDFs for particles outside the recirculation bubble are shown in Figs. 12(b), 12(d), 12(f), and 12(h) relative to St=0.1, St=0.5, St=1, and St=2.0 particles, respectively. Statistics shown in Fig. 12 are calculated averaging over a given time interval. We calculated the same statistics for a large number of different time intervals and we obtained no significant difference suggesting that the behavior of the particles is maintained during the entire time span covered by the simulation.

PDFs have a larger spreading and sample also regions of positive Q. Again, we can observe a peak at $Q=0$. However, the interesting result is that each PDF is characterized by a second peak shifted towards values of negative Q and centered at $Q^* \simeq -0.04$, the height of which changes nonmonotonically with particle inertia. The presence of a secondary peak indicates that, in the near-wall region outside the recirculation bubble, particles sample preferentially regions where straining motions dominate vorticity. If we characterize all coherent structures with isosurfaces of the streamline rotation vector, which we consider a better vortex identifier than Q itself as it provides information about the rotation of vortical structures,[1,50] we find that the structures populating flow regions where $Q=Q^*$ are precisely those shown (at different time instants) in Figs. 7 and 9. These structures have size, shape, and orientation that resemble very closely those shown by De Angelis *et al.*,[1] Calhoun and Street,[17] and Tseng and Ferziger.[51]

D. Remarks on particle deposition

As mentioned in Sec. I, predicting the deposition rate of small particles or droplets dispersed in a turbulent gas flow
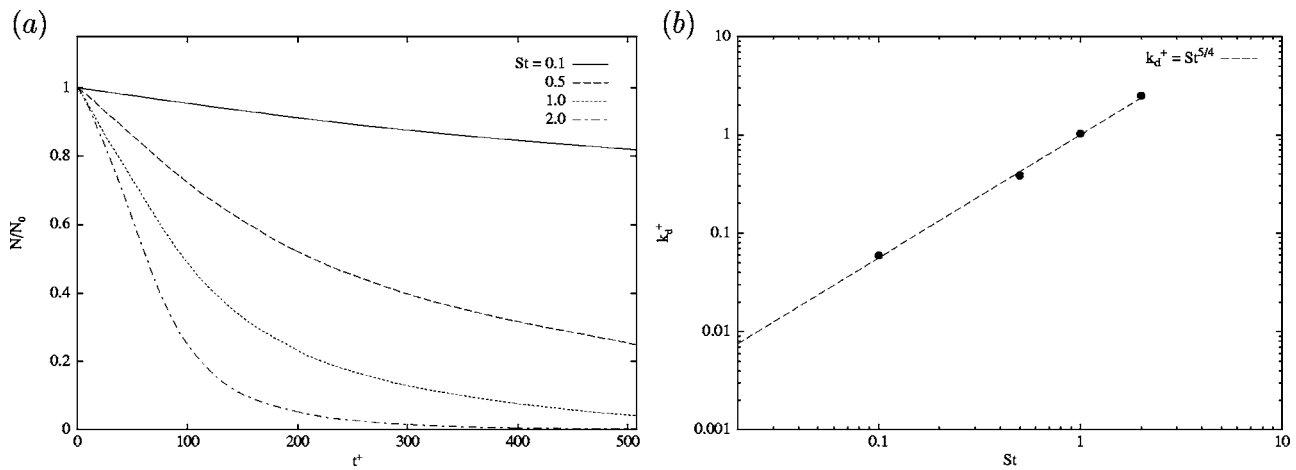
FIG. 13. (a) Decrease of particle number in time due to deposition ($N_0 = 10^5$) and (b) deposition coefficients as a function of the particle Stokes number (St).

over wavy walls has practical relevance in many engineering applications. A wealth of literature data for the case of flat plate boundary layer in vertical and horizontal channel or pipe exists, which has been critically examined by Young and Leeming.[52] However, there is a lack of data for the case of wavy channels, where deposition is influenced by different classes of vortical structures spanning a wide range of spatial and temporal scales. In this section, a preliminary assessment of the impact of the wall waviness on particle deposition rate is made.

The turbulent mass transport equation included in the model by Cousins and Hewitt[53] states that the particle deposition flux (J) is proportional to particle concentration (C) and to the area of deposition (A_d). The flux J is the rate at which noninteracting particles deposit (dN/dt) while particle concentration C is defined as the ratio between the number of particles and the occupied volume (N/ϕ). We can thus write

$$\frac{dN}{dt} = -k_d \frac{N A_d}{\phi}, \tag{11}$$

where the deposition coefficient k_d is the constant of proportionality. Given the initial number N_0 of particles released in the channel and the number $N(t)$ of particles already deposited at a given time t, integration of Eq. (11) yields the following nondimensional expression:

$$\frac{N(t^+)}{N_0} = \exp\left(\frac{-k_d^+ t^+}{\mathrm{Re}_\tau}\right), \tag{12}$$

where k_d^+ is the nondimensional deposition coefficient. Calculations were made imposing the condition of perfectly absorbing wall:[54] particles are labeled as deposited even if they are subsequently reentrained in the outer flow. To separate the outer flow region from the deposition region, we have identified a fictitious wavy surface at a distance of one non-dimensional particle radius from the bottom wall.

According to Eq. (12), the deposition coefficient can be obtained from the profiles for the decrease of particle number in time due to deposition, $N(t)/N_0$. In Fig. 13(a), these profiles are shown in a semilog plot. After 500 t^+, almost all St=2.0 and St=1.0 particles and more than 75% of St=0.5

particles have deposited. As expected, only 20% of St=0.1 particles have deposited during the same time interval. The slope at the linear part of each profile gives the constant value for k_d^+, which represents particle deposition velocity and can be used to quantify the rate of particle deposition on the wavy wall. Note that, depending on particle size, constant deposition rates are attained at different times.

In Fig. 13(b), we show the deposition rates as a function of particle Stokes number. These rates are usually divided into different regimes depending on particle size. All particle sets considered in the present study fall into the so-called *diffusion-impaction* regime ($0.1 < \mathrm{Re} < 20$).[52] This regime is characterized by an increase in deposition rate of several orders of magnitude, due to the interaction between particles having significant inertia and the coherent vortical structures.[52] In Fig. 13(b), larger values of the nondimensional deposition coefficient actually correspond to larger particles and the observed increase can be modeled in terms of particle Stokes number by a relation of the form

$$k_d^+ = \alpha \cdot \mathrm{St}^\beta, \tag{13}$$

where α and β are numerical constants ($\alpha = 1$ and $\beta = 5/4$ in the present case).

Visual comparison with the literature experimental data collected in Young and Leeming[52] indicates that the values of k_d^+ reported in Fig. 13(b) are two orders of magnitude larger than those for particle deposition from fully developed turbulent pipe/channel flow, suggesting that modifications in boundary layer turbulence by wavy walls increase dramatically particle deposition.

IV. CONCLUSIONS AND FUTURE DEVELOPMENTS

The mechanisms which control particle/droplet deposition and resuspension in a turbulent flow over a wavy wall are of crucial importance to control momentum, heat and mass transfer rates. Practical applications range from corrosion and fouling in undulated heat exchangers, condensers and evaporators to gas transfer at ocean/atmosphere interface and to formation, erosion, and dynamics of undersea or desert sand dunes.

The turbulent flow over a wavy wall displays complex spatial and temporal vortical structures spanning a wide range of scales. Yet typical boundary layer coherent structures can be identified as quasistreamwise vortices growing up on the upslope side of the wave and interacting with geometry-dependent spanwise-aligned vortices, located within the recirculation bubble in the wave trough. The nonlinear interaction between these vortices creates the conditions for the development of a three-dimensional highly turbulent field, in which particles are seen to disperse, cluster, and preferentially accumulate. This macroscopic particle behavior can be described in connection with the mean features of the flow field.

In this paper, we used LES coupled with Lagrangian particle tracking to examine particle deposition and resuspension mechanisms in connection with the dynamics of the coherent structures. The present study confirms that there are two distinct flow regions: one extending from the separation point to the reattachment point, which acts as a pocket where particles fall and finally deposit after being entrained by the recirculation bubble, and one extending from reattachment to separation, in which particles are actively deposited and resuspended by the quasistreamwise vortices.

Particles driven to the wall are seen to accumulate and segregate into specific regions of the flow. This is particularly true when the response time of the particles, quantified by their Stokes number St, is comparable to the flow structures time scales, as suggested also by similar analysis in different flow configurations. Therefore, we tried to identify the flow time scales that control dispersion and segregation quantifying the degree of preferential particle distribution. To this end, we used the second invariant of the velocity gradient tensor.

We verified the tendency of inertial particles to collect in high-strain low-vorticity near-wall flow regions, first observed by Squires and Eaton.[48] We have also shown that the processes of deposition, segregation, and resuspension are the result of the selective response of particles to the underlying flow field. This response strongly depends on particle inertia, the particle-to-fluid Stokes number being the controlling parameter. Inertia acts as a low-pass filter, weakening the effect of coherent wall structures and reducing the degree of particle segregation.

We also tried to provide practical-type applications for engineering use. We quantified the deposition rate depending on the Stokes number. Results show that modifications of the local flow field induced by the presence of a wavy wall significantly increase the deposition rate by several orders of magnitude with respect to the case of a flat wall. In particular, for the particle sizes considered here the nondimensional deposition coefficient is a monotonically increasing function of the Stokes number.

ACKNOWLEDGMENTS

[1] V. De Angelis, P. Lombardi, and S. Banerjee, "Direct numerical simulation of turbulent flow over a wavy wall," Phys. Fluids **9**, 2429 (1997).

[2] C. Marchioli and A. Soldati, "Mechanisms for particle transfer and segregation in turbulent boundary layer," J. Fluid Mech. **468**, 283 (2002).

[3] F. Sbrizzai, R. Verzicco, M. Pidria, and A. Soldati, "Mechanisms for selective radial dispersion of microparticles in the transitional region of a confined turbulent round jet," Int. J. Multiphase Flow **30**, 1389 (2004).

[4] M. Picciotto, C. Marchioli, and A. Soldati, "Characterization of near-wall accumulation regions for inertial particles in turbulent boundary layers," Phys. Fluids **17**, 098101 (2005).

[5] B. J. Boersma, "Particle distribution in the flow over a wavy wall," *Proceedings of Summer School 2000*, Center for Turbulence Res. (CTR), Stanford University (2000), pp. 109–117.

[6] S. Leibovich, "The form and dynamics of Langmuir circulations," Annu. Rev. Fluid Mech. **15**, 391 (1983).

[7] W. Gong, P. A. Taylor, and A. Dornbrack, "Turbulent boundary-layer flow over fixed aerodynamically rough two-dimensional sinusoidal waves," J. Fluid Mech. **312**, 1 (1995).

[8] P. Cherukat, Y. Na, T. J. Hanratty, and J. B. McLaughlin, "Direct numerical simulation of a fully developed flow over a wavy wall," Tech. Dig. - Int. Electron Devices Meet. **11**, 109 (1998).

[9] Y. S. Chang and A. Scotti, "Entrainment and suspension of sediments into a turbulent flow over ripples," J. Turbul. **4**, 1 (2003).

[10] V. Armenio and U. Piomelli, "A Lagrangian mixed subgrid-scale model in generalized coordinates," Flow, Turbul. Combust. **65**, 51 (2000).

[11] J. D. Hudson, L. Dykhno, and T. J. Hanratty, "Turbulence production in flow over a wavy wall," Exp. Fluids **20**, 257 (1996).

[12] M. V. Salvetti, R. Damiani, and F. Beux, "Three-dimensional coarse large-eddy simulations of the flow above two-dimensional sinusoidal waves," Int. J. Numer. Methods Fluids **35**, 617 (2001).

[13] Y. Zang, R. L. Street, and J. R. Koseff, "A non-staggered grid, fractional step method for time-dependent incompressible Navier-Stokes equations in curvilinear coordinates," J. Comput. Phys. **114**, 18 (1994).

[14] M. V. Salvetti and S. Banerjee, "A-priori tests of a new dynamic subgrid-scale model for finite-difference large-eddy simulations," Phys. Fluids **7**, 2831 (1995).

[15] M. Germano, U. Piomelli, P. Moin, and W. H. Cabot, "A dynamic subgrid-scale eddy-viscosity model," Phys. Fluids A **3**, 1760 (1991).

[16] Y. Zang and R. L. Street, "A composite multigrid method for calculating unsteady incompressible flows in geometrically complex domains," Int. J. Numer. Methods Fluids **20**, 341 (1995).

[17] R. Calhoun and R. L. Street, "Turbulent flow over a wavy surface. Part 1: Neutral case," J. Geophys. Res. **106**, 9277 (2001).

[18] S. E. Belcher and J. C. R. Hunt, "Turbulent flow over hills and waves," Annu. Rev. Fluid Mech. **30**, 507 (1998).

[19] D. S. Henn and I. R. Sykes, "Large-eddy Simulation of flow over wavy surface," J. Fluid Mech. **383**, 75 (1999).

[20] P. P. Sullivan, J. C. McWilliams, and C.-H. Moeng, "Simulation of turbulent flow over idealized water waves," J. Fluid Mech. **404**, 47 (2000).

[21] C. Maaß and U. Schumann, "Direct numerical simulation of separated turbulent flow over a wavy boundary," in *Flow Simulation with High Performance Computers*, edited by E. H. Hirschel, Notes on Numerical Fluid Mechanics Vol. 52 (Vieweg Verlag, Braunschweig, 1996), p. 227.

[22] A. Soldati, "On the effects of electrohydrodynamic flows and turbulence on aerosol transport and collection in wire-plate electrostatic precipitators," J. Aerosol Sci. **31**, 293 (2000).

[23] M. Campolo, M. V. Salvetti, and A. Soldati, "Mechanisms for microparticle dispersion in a jet in crossflow," AIChE J. **51**, 28 (2005).

[24] V. Armenio, U. Piomelli, and V. Fiorotto, "Effect of the subgrid scales on particle motion," Phys. Fluids **11**, 3030 (1999).

[25] M. R. Maxey and J. J. Riley, "Equation of motion for a small rigid sphere in a nonuniform flow," Phys. Fluids **26**, 883 (1983).

[26] S. E. Elghobashi and G. C. Truesdell, "Direct simulation of particle dispersion in a decaying isotropic turbulence," J. Fluid Mech. **242**, 655 (1992).

[27] J. N. Chung and T. R. Troutt, "Simulation of particle dispersion in an axisymmetric jet," J. Fluid Mech. **186**, 199 (1988).

[28] E. Loth, "Numerical approaches for motion of dispersed particles, droplets and bubbles," Prog. Energy Combust. Sci. **26**, 161 (2000).

[29] V. Armenio and V. Fiorotto, "The importance of the forces acting on particles in turbulent flows," Phys. Fluids **13**, 2437 (2001).

[30] P. N. Rowe and G. A. Enwood, "Drag forces in hydraulic model of a fluidized bed—Part I.," Trans. Inst. Chem. Eng. **39**, 43 (1962).

[31] P. G. Saffman, "The lift on a small sphere in a slow shear flow," J. Fluid Mech. **22**, 385 (1965); [Corrigendum, *ibid.* **31**, 624 (1968)].

[32] J. B. McLaughlin, "Inertial migration of a small sphere in linear shear flows," J. Fluid Mech. **224**, 261 (1991).

[33] J. B. McLaughlin, "The lift on a small sphere in wall-bounded linear shear flows," J. Fluid Mech. **246**, 249 (1993).

[34] E. A. Fadlun, R. Verzicco, P. Orlandi, and J. Mohd-Yusof, "Combined immersed-boundary/finite-difference methods for three-dimensional complex flow simulations," J. Comput. Phys. **161**, 35 (2000).

[35] S. Nakagawa, Y. Na, and T. J. Hanratty, "Influence of a wavy boundary on turbulence. I. highly rough surface," Exp. Fluids **35**, 422 (2003).

[36] J. Buckles, T. J. Hanratty, and R. J. Adrian, "Turbulent flow over large-amplitude wavy surfaces," J. Fluid Mech. **140**, 27 (1984).

[37] J. D. Kuzan and T. J. Hanratty, "Turbulent flows with incipient separation over solid waves," Exp. Fluids **7**, 88 (1989).

[38] S. Nakagawa and T. J. Hanratty, "Particle image velocimetry measurements of flow over a wavy wall," Phys. Fluids **13**, 3504 (2001).

[39] A. Günther and R. P. von Rhor, "Large-scale structures in a developed flow over a wavy wall," J. Fluid Mech. **478**, 257 (2002).

[40] B. van Haarlem, B. J. Boersma, and F. T. M. Nieuwstadt, "Direct numerical simulation of particle deposition onto a free-slip and no-slip surface," Phys. Fluids **10**, 2608 (1998).

[41] A. Perry and M. S. Chong, "A description of eddying motions and flow patterns using critical point concepts," Annu. Rev. Fluid Mech. **9**, 125 (1987).

[42] J. W. Brooke, K. Kontomaris, T. J. Hanratty, and J. B. McLaughlin, "Turbulent deposition and trapping of aerosols at a wall," Phys. Fluids A **4**, 825 (1992).

[43] The deviation of particle distribution from randomness, D, is obtained comparing the actual histograms of particle number density computed on a regular grid of boxes with Poisson distribution of the same mean. The value of D varies with the box width used for the calculation: at very small and very large scales, there exists no mechanisms to preferentially concentrate particles so D should be zero in these limiting cases; as preferential concentration does occur at some scale, this necessitates at least one local maximum for D. Thus, we must find the box width corresponding to maximum particle organization to obtain such maximum.

[44] D. W. I. Rouson and J. K. Eaton, "On the preferential concentration of solid particles in turbulent channel flow," J. Fluid Mech. **428**, 149 (2001).

[45] J. R. Fessler, J. D. Kulick, and J. K. Eaton, "Preferential concentration of heavy particles in a turbulent channel flow," Phys. Fluids **6**, 3742 (1994).

[46] J. K. Eaton and J. R. Fessler, "Preferential concentration of particles by turbulence," Int. J. Multiphase Flow **20**, 169 (1994).

[47] M. R. Maxey, "The gravitational settling of aerosol particles in homogeneous turbulence and random flow fields," J. Fluid Mech. **174**, 441 (1987).

[48] K. D. Squires and J. K. Eaton, "Preferential concentrations of particles by turbulence," Phys. Fluids A **3**, 1169 (1990).

[49] M. S. Chong, A. E. Perry, and B. J. Cantwell, "A general classification of three-dimensional flow fields," Phys. Fluids A **2**, 765 (1990).

[50] J. Jeong and F. Hussain, "On the identification of a vortex," J. Fluid Mech. **285**, 69 (1995).

[51] Y.-H. Tseng and J. H. Ferziger, "Large-eddy simulation of turbulent wavy flow—illustration of vortex dynamics," J. Turbul. **5**, 034 (2004).

[52] J. Young and A. Leeming, "A theory of particle deposition in turbulent pipe flow," J. Fluid Mech. **340**, 129 (1997).

[53] L. B. Cousins and G. F. Hewitt, "Liquid phase mass transfer in annular two-phase flow," UKAEA Report No. AERE-R 5657 (1968).

[54] W. S. J. Uijttewaal and R. V. A. Oliemans, "Particle dispersion and deposition in direct numerical and Large Eddy Simulation of vertical pipe flows," Phys. Fluids **8**, 2590 (1996).